

Realistic Total-Body J-PET Geometry Optimization - Monte Carlo Study

Jakub Baran^{1,2,3}, Wojciech Krzemien^{4,2,3}, Szymon Parzych^{1,2,3}, Lech Raczyński⁵, Mateusz Bała⁵, Aurélien Coussat^{1,2,3}, Neha Chug^{1,2,3}, Eryk Czerwiński^{1,2,3}, Catalina Oana Curceanu⁶, Meysam Dadgar^{1,2,3}, Kamil Dulski^{1,2,3}, Kavya Eliyan^{1,2,3}, Jan Gajewski⁷, Aleksander Gajos^{1,2,3}, Beatrix C. Hiesmayr⁸, Krzysztof Kacprzak^{1,2,3}, Łukasz Kapłon^{1,2,3}, Konrad Klimaszewski⁵, Grzegorz Korcyl^{1,2,3}, Tomasz Kozik^{1,2,3}, Deepak Kumar^{1,2,3}, Szymon Niedźwiecki^{1,2,3}, Dominik Panek^{1,2,3}, Elena Perez del Rio^{1,2,3}, Antoni Ruciński⁷, Sushil Sharma^{1,2,3}, Shivani^{1,2,3}, Roman Y. Shopa⁵, Magdalena Skurzok^{1,2,3}, Ewa Stępień^{1,2,3}, Faranak Tayefiardebili^{1,2,3}, Keyvan Tayefiardebili^{1,2,3}, Wojciech Wiślicki⁵, Paweł Moskal^{1,2,3}

¹Faculty of Physics, Astronomy and Applied Computer Science, Jagiellonian University, Kraków, Poland ²Total-Body Jagiellonian-PET Laboratory, Jagiellonian University, Kraków, Poland ³Center for Theranostics, Jagiellonian University, Kraków, Poland ⁴High Energy Physics Division, National Centre for Nuclear Research, Otwock-Świerk, Poland ⁵Department of Complex Systems, National Centre for Nuclear Research, Otwock-Świerk, Poland ⁶INFN, Laboratori Nazionali di Frascati, Frascati, Italy ⁷Institute of Nuclear Physics Polish Academy of Sciences, Kraków, Poland ⁸Faculty of Physics, University of Vienna, Vienna, Austria

Author to whom correspondence should be addressed. email: jakubbaran92@gmail.com, wojciech.krzemien@ncbj.gov.pl

Abstract

Background: Total-Body PET is one of the most promising medical diagnostics modalities, opening new perspectives for personalized medicine, low-dose imaging, multi-organ dynamic imaging or kinetic modelling. The high sensitivity provided by Total-Body technology can be advantageous for novel tomography methods like positronium imaging, demanding the registration of triple coincidences. Currently, state-of-the-art PET scanners use inorganic scintillators. However, the high acquisition cost reduces the accessibility of Total-Body PET technology. Several efforts are ongoing to mitigate this problem. Among the alternatives, the Jagiellonian PET (J-PET) technology, based on axially arranged plastic scintillator strips, offers a low-cost alternative

solution for Total-Body PET.

Purpose: The work aimed to compare five Total-Body J-PET geometries with plastic scintillators suitable for multi-organ and positronium tomography as a possible next-generation J-PET scanner design.

Methods: We present comparative studies of performance characteristics of the cost-effective Total-Body PET scanners using J-PET technology. We investigated *in silico* five Total-Body scanner geometries, varying the number of rings, scanner radii, and other parameters. Monte Carlo simulations of the anthropomorphic XCAT phantom, the extended 2-meter sensitivity line source and positronium sensitivity phantoms were used to assess the performance of the geometries. Two hot spheres were placed in the lungs and in the liver of the XCAT phantom to mimic the pathological changes. We compared the sensitivity profiles and performed quantitative analysis of the reconstructed images by using the quality metrics such as contrast recovery coefficient, background variability and root mean squared error. The studies are complemented by the determination of sensitivity for the positronium lifetime tomography and the relative cost analysis of the studied setups.

Results: The analysis of the reconstructed XCAT images reveals the superiority of the seven-ring scanners over the three-ring setups. However, the three-ring scanners would be approximately 2-3 times cheaper. The peak sensitivity values for two-gamma vary from 20 to 34 cps/kBq and are dominated by the differences in geometrical acceptance of the scanners. The sensitivity curves for the positronium tomography have a similar shape to the two-gamma sensitivity profiles. The peak values are lower compared to the two-gamma cases, from about 20-28 times, with a maximum value of 1.66 cps/kBq. This can be contrasted with the 50-cm one-layer J-PET modular scanner used to perform the first in-vivo positronium imaging with sensitivity of 0.06 cps/kBq.

Conclusions: The results show the feasibility of multi-organ imaging of all the systems to be considered for the next generation of TB J-PET designs. Among the scanner parameters, the most important ones are related to the axial field-of-view coverage. The two-gamma sensitivity and XCAT image reconstruction analyses show the advantage of seven-ring scanners. However, the cost of the scintillator materials and SiPMs is more than two times higher for the longer modalities compared to the three-ring solutions. Nevertheless, the relative cost for all the scanners is about 10-4 times lower compared to the cost of the uExplorer. These properties coupled together with J-PET cost-effectiveness and triggerless acquisition mode enabling three-gamma positronium imaging, make the J-PET technology an attractive solution for broad application in clinics.

1. Introduction

Positron emission tomography (PET) is a gold standard diagnostic modality enabling metabolic imaging of pathological tissues¹⁻³. Presently, the majority of PET machines offer an axial Field-Of-View (FOV) of approximately 20-25 cm with a single bed position. To perform an image of the entire patient's body, a series of scans acquired with different bed positions is necessary. The new generation of Total-Body (TB) PET scanners⁴⁻⁷ allows for simultaneous imaging of the whole human body, presenting new perspectives in dynamic imaging, kinetic modelling⁸⁻¹¹, positronium lifetime imaging¹²⁻¹⁴, and simultaneous multi-tracer imaging¹⁵.

The usage of inorganic L(Y)SO scintillators, while popular, results in high costs of the existing TB scanners, estimated to be in the range of about \$10 million or more¹⁶. The high price reduces the accessibility of TB technology for hospitals and research facilities. To reduce the TB scanner cost⁹, various approaches have been proposed, including the reduction of the scintillator thickness^{17,18}, rearrangement of the scintillators to the sparse configurations^{19,20}, use of the BGO crystals combined with the Cherenkov photon signal measurement for timing information^{21,22} or the use of plastic scintillators^{23,24}. The use of plastic scintillators substantially decreases the price, as they are more than an order of magnitude less expensive than L(Y)SO crystals.²⁵ Moreover, the cylindrical arrangement of the long scintillator strips allows the positioning of the readouts mainly at the ends of the cylindrical rings in contrast to crystal-based PET detectors where coverage of the full cylindrical surface is necessary. In consequence, the amount of required silicon photomultipliers (SiPMs), which constitute an important part of the overall scanner price, are greatly reduced.

A cost-effective, portable and modular PET scanner (J-PET) with an extended 50-cm long Axial Field of View (AFOV) is currently in operation at the Jagiellonian University in Kraków.²⁶ The application of the J-PET scanner extends beyond the standard medical two-photon imaging²⁴. It provides the capability to conduct multi-gamma tomography studies such as positronium imaging¹² and simultaneous multi-tracer imaging¹⁵. Furthermore, it is utilized in fundamental physics studies on quantum entanglement²⁷ and studies of discrete symmetries in nature^{28,29}. Additionally, it is used in proton beam range monitoring in hadron radiotherapy³⁰⁻³³, and PET data reconstruction methods development^{34,35}.

The primary objective of this study is to analyse and compare the performance of five realistic geometry options for designing the new Total-Body (TB) modality based on the J-PET modular technology. The main functional goal is to develop a cost-effective prototype designed to leverage the TB scanner technology, enabling e.g. multi-organ imaging. Simultaneously, the sensitivity should allow performing positronium mean lifetime tomography which can deliver complementary information to the currently used standardized uptake value image [12,36,37](#).

For further insights into the potential clinical applications of J-PET technology, detailed information can be found in the article [25](#).

The selection of the particular tested designs including scintillator lengths, gaps between detectors and radii is driven by the constraints imposed by the physical properties of currently available scintillators, the shape of the front-end electronics, and photomultipliers. Special emphasis is put on the realism of the modelled geometries, with attention to many details abstracted in previous studies. E.g. the previous studies used idealized cylinders with tightly placed scintillators. To make the simulation conditions more realistic, we take into account the size of the front-end electronics, and the gaps between adjacent rings, as well as inactive detector material. It has been shown that larger gaps are feasible for 3D PET and can be particularly effective in the design of TB-PET scanners [38,39](#). Additionally, the length of the scintillator strips is restricted to 686.4 mm and 330.0 mm, to improve the time resolution and light yield in the scintillator which is strongly attenuated in longer strips [40](#). In consequence, longer scanners are constructed by combining adjacent rings of cylindrical strips.

We also introduce the Wavelength Shifter (WLS) layer which improves the precision of the reconstructed position along the scintillator strip [40](#). We developed dedicated GATE modules to handle the details of the new geometry including the WLS. In contrast to previous studies [23,24](#), our current work centres on the assessment of the quality of the reconstructed images based on the Monte Carlo simulations of the extended cardiac-torso phantom (XCAT). Furthermore, we expand the previously used metrics such as contrast recovery coefficient (CRC) and background variability (BV), by adding the Root Mean Square Error (RMSE), and the Q metric which combines the CRC and BV. Another innovation involves the implementation and application of the bootstrap list-mode method to estimate the metric uncertainty. Our studies are supplemented by the sensitivity curves for the conventional

two-gamma tomography, as well as for the positronium mean lifetime tomography.

Based on the performed analysis, the TB J-PET scanner setups are compared. Currently, works toward the construction of the TB J-PET scanner are ongoing^{24,41,42}.

II. Materials and Methods

II.A. Monte Carlo simulation parameters

J-PET scanner geometries were modelled using GATE v9.0^{43,44}, based on Geant v4.10.7.1⁴⁵. An additional layer of Wave Length Shifters (WLS), which improves the estimation of the axial coordinate of the photon interaction point⁴⁰, was incorporated into the simulation model. The default GATE digitizer code was extended by a dedicated module to allow the simulation of the signals registered in the WLS layers. In all the simulations the `em_livermore_polar` physics list was used, which is the standard choice for all J-PET-related MC simulations²⁴. The tracking of optical photons was not included in the simulations to reduce the computation time. In the XCAT and conventional sensitivity simulations, the β^+ source decay is not simulated directly and simulation starts at the emission of the back-to-back photon pairs.

II.B. Phantoms

We simulated XCAT⁴⁶, the extended sensitivity²⁴ and the positronium sensitivity phantoms. The activity of the male XCAT phantom⁴⁶ was prepared^{47,48} to mimic the ^{18}F -FDG distribution within the human body. Additionally, two hot spheres (diameter = 1.0 cm) positioned in the lung and in the liver were incorporated in the phantom simulations. The contrast between the hot region and the background activity was set to 16:1 and 3:1 for the lungs and liver, respectively. The overall activity of the phantom was equal to 50 MBq and the acquisition time was set to 600 s.

The extended sensitivity phantom consists of the 2-meter linear source positioned in the centre, along the long axis of the cylindrical scanner. For each simulation, the activity of 10 MBq and measurement time of 1000 s were used.

For the aforementioned scanners, the back-to-back 511 keV gamma source has been used.

Additionally, the positronium sensitivity phantom consists of a 183 cm-long linear source situated in the transaxial centre of the scanner. In the simulation, the ^{44}Sc -like source was modelled by using a para-positronium source with enabled deexcitation photon of energy set to 1160 keV.

III. Total-Body J-PET scanner geometries

Five TB J-PET scanner configurations were studied. Scanners with varying numbers of rings, the length of the gap between the subsequent rings, scanner radii, and scintillator cross-sections were investigated. The selection of these specific designs, such as scintillator lengths, gaps between detectors, and radius was determined by the constraints imposed by the physical properties of the available scintillators and photomultipliers, dimensions and shape of the front-end electronics, and other materials.

All total-body geometry scanners under consideration are based on the J-PET portable module concept - an independent detection unit composed of plastic scintillator strips (see Fig. 1 left Panel). The chemical composition of the scintillator corresponds to the commercial EJ230 scintillator, which is used in the existing J-PET scanner prototypes^{12,24}. The annihilation photons passing through the plastic scintillator strips interact predominately via Compton scattering. Deposited energy is converted into scintillation light which is then collected at the ends of the scintillators by the SiPMs and read out by fast, customized on-board front-end electronics enabling time-of-flight (TOF) measurement⁴⁹. The modules were placed as closely as possible to the front-end electronics configuration. Each ring consists of 24 modules arranged cylindrically. The length of the scintillator strips is restricted to 686.4 mm and 330.0 mm, to improve the time resolution and light yield in the scintillator which is strongly attenuated in longer strips⁴⁰. The dependence of time resolution on strip length was incorporated into the simulation model. The longer scanners are constructed by combining adjacent rings of cylindrical strips (see Fig. 1 Right Panel). The plastic scintillators are approximately 7 times less dense than LYSO crystals, and hence less effective for registering annihilation photons. We use two layers to compensate for the lower stopping power of the plastic scintillators. Adding more layers would increase the cost. To enhance the precision of the reconstructed position along the scintillator strip, each module is equipped with a layer of WLSs⁴⁰.

In all cases, the modules were placed as close to each other as possible with respect to the electronics configuration. The radius difference between S1-S3 and S4-S5 is determined by the larger module cross-section, which required more space and in consequence significantly greater radius compared to the S3-S5 setups. In both cases, the scintillator cross section is set to fit the size of the SiPM active surface equal to $6 \times 6 \text{ mm}^2$.

The selection of these scanner geometries allows for studying the impact of several parameters (see Tab. 1) on the system performance. Scanners S1 and S2 give insight into the influence of the gap between the rings. The 2 cm gap corresponds to the smallest mechanically possible distance, where all the front-end electronics components are tightly packed, while the 5 cm space allows for some flexibility in the mechanical construction. The difference between the S1 and S3 modalities consists mainly of the two radius values. The use of a smaller radius permits decreasing the number of readout channels, enhances geometrical angle coverage, and leads to better sensitivity. On the other hand, a scanner design with a larger diameter leaves more space between the modules simplifying the mechanical support. The larger diameter, especially in the case of the TB scanners, has the additional advantage of improving the patient's comfort during the scan, by lowering anxiety and reducing claustrophobia, which is one of the psychological burdens the patient must face during medical examination^{50,51}. The S4 and S5 scanners are used to study the effect of the scintillator width. Finally, the S3 and S4 modalities have different cross-sections and use different scintillator lengths resulting in changes in timing resolution^{23,24}.

The price of the considered J-PET scanners was estimated using the methodology inspired by the work⁸. The overall cost of the TB scanner can be decomposed into (a) the cost of the CT system, (b) the cost of scintillator materials, (c) the cost of the front-end electronics boards, and (d) the cost of the SiPMs. The prices of the electronic boards (c) and CT scanners (a) are assumed to be similar for all TB systems. The plastic scintillators are about 80 times less expensive than L(Y)SO crystals for the 1 cm^3 volume. In addition, the cylindrical arrangement of the long scintillator strips allows the SiPMs only at the ends, reducing their number. For each scanner setup, we calculate the overall volume of the scintillator materials. Moreover, we include WLS layer volume, assuming that the material per volume is 4 times more expensive than the plastic scintillator price. We also estimate the number of required SiPMs by calculating the area covered by them. Taking into account (b) and (d) terms, we estimate the price reduction factor for J-PET scanner setups. As

a reference point, we take the material budget of the uExplorer scanner⁵. Therefore, if a scanner has a price reduction factor equal to 2 it means that it would be two times cheaper than uExplorer in terms of overall SiPMs and scintillator price.

Table 1: Scanners properties. As a reference point for the price reduction factor, we take the material budget of the uExplorer scanner.

Property	Scanner geometry				
	<i>S1</i>	<i>S2</i>	<i>S3</i>	<i>S4</i>	<i>S5</i>
Radius [mm]	506	506	425	414.65	414.65
Axial FOV [mm]	2099.2	2159.2	2099.2	2430	2430
Scintillator length [mm]	686.4	686.4	686.4	330	330
Scintillator cross-section [mm]	25x5.7	25x5.7	25x5.7	25x6.0	30x6.0
No of adjacent rings	3	3	3	7	7
Gap between adjacent rings [mm]	20	50	20	20	20
Price reduction factor	9.6	9.6	9.6	4.3	3.6

III.A. Photon detection, coincidence formation and energy threshold

The front-end electronic response was modelled by the GATE digitizer which converts photon interaction in the scintillator into deposited energy and detection time.

The temporal and energy resolution of the scanner was described by the phenomenological parameterisation of the experimental resolutions. The energy resolution dependence is parameterised as a $\frac{\sigma(E)}{E}$ fraction which reflects the experimentally determined relation for the plastic scintillator strips⁵². The simulated photon registration time is smeared, event by event, by replacing the event registration time t_r by the value obtained from the normal distribution $N(t_r, \sigma_t)$, where σ_t corresponds to the temporal resolution of the scintillator strip. Analogically, the registration position along the scintillator strip (z position) is smeared, event by event, by replacing the registered photon position z by the value obtained from the normal distribution $N(z, \sigma_z)$, where σ_z corresponds to the positional uncertainty along the scintillator strip of the scanner. For all the simulations the resolution parameters, i.e., the position along the strip and the time were set to σ_z equal to 2.12 mm²⁴ and σ_t equal to 100 ps

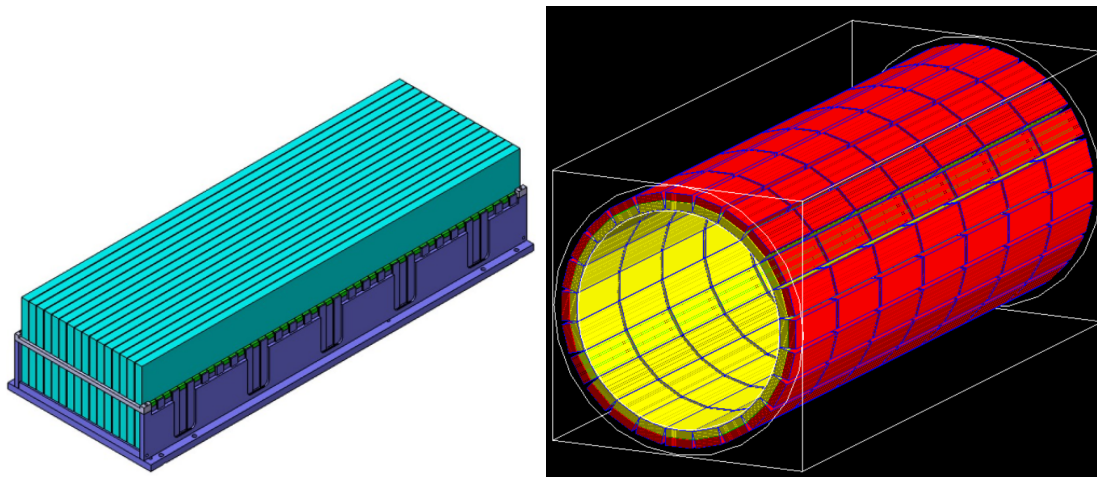


Figure 1: (Left) Visualization of the single module, made of plastic scintillators (light blue) with the WLS layer (green elements) and the casing (violet - not included in the simulation model). (Right) Visualisation of the seven-ring S5 scanner with a total FOV of 243 cm. The length of the scintillators in each ring is equal to 33 cm. The gap between adjacent rings is equal to 2 cm. Two layers of the scanners are shown (yellow and red strips).

(scanners S1, S2 and S3) or 77 ps (scanners S4 and S5)⁵³, respectively. Discrepancies in time smoothing reflect the expected time resolution change due to the size of the scintillator strip length^{24,54,55}.

In the case of the XCAT and extended sensitivity phantoms the coincidence time window of 3 ns was used. In contrast to the inorganic detectors, in plastic scintillators, the photons deposit their energy mainly via Compton scattering. The energy selection threshold E_{thr} of 200 keV was set to reduce the fraction of the background coincidence events^{23,24}, for which at least one of them undergoes the scattering in the phantom before being registered in the scanner. Only coincidence pairs with the registration photon energy above the energy threshold are considered. This selection criterion corresponds to the optimal selection cut applied in the analysis of the data obtained with the J-PET prototype allowing for the reduction of scattering in the patient and the detectors^{23,24,52}.

For the positronium imaging sensitivity analysis, simulated interactions were further processed by the external coincidence sorter allowing triple coincidence formation. A valid positronium coincidence was defined as two photons originating from the annihilation registered in the deposited energy range from 200 keV to 350 keV, combined with the third photon registration with the deposited energy above 350 keV. Such triple had to be in coincidence

within a 3-ns time window. Additionally, to obtain only true coincidences, conditions such as: originating from the same annihilation-deexcitation event or lack of prior interactions of any of the three photons were applied.

III.B. Data preselection and preparation

For the image reconstruction analysis, only true coincidences were taken into account.

The background and contrast 3D region-of-interests (ROIs) were used for the image quality metrics determination. ROIs for the quantitative analysis did not include the whole hot region but were morphologically eroded to overcome the partial volume effects. 15 background ROIs were chosen separately for the liver and lung regions. Both, hot sphere and background ROIs, are composed of 52 voxels. To avoid the partial volume effect, an additional constraint, that the background ROI cannot be neighbouring the region of different activities, was applied⁵⁶.

III.C. PET image reconstruction

The image reconstruction was performed with the CASToR software package⁵⁷. TOF List Mode - Maximum Likelihood Expectation Maximization algorithm with 150 iterations was used. The reconstruction voxel size was $2.5 \times 2.5 \times 2.5 \text{ mm}^3$. TOF resolution kernel was modelled as the Gaussian function. Sensitivity and attenuation corrections were included. The multi-Siddon projector with 10 rays was used. Reconstructed images were smoothed with 3D Gaussian post-filter with σ set to 2.5 mm. No additional resolution modelling was used in the reconstruction process.

III.D. TOF resolution optimization

The CASToR software provides the possibility to use the shift-invariant TOF kernel only. This approach can be sub-optimal, especially while dealing with large FOV scanners, where the kernel shape can change significantly in the axial direction^{58,59}. However, the aim of these studies is the relative performance comparison between scanner configurations, and the usage of the shift-invariant TOF kernel will affect all the investigated setups in a rather equal manner.

In the J-PET scanners, the TOF resolution is affected by the additional hit registration uncertainty along the axial direction of the strip that effectively smears the overall TOF resolution (see Fig. 2). More details can be found in the supplementary materials. As a

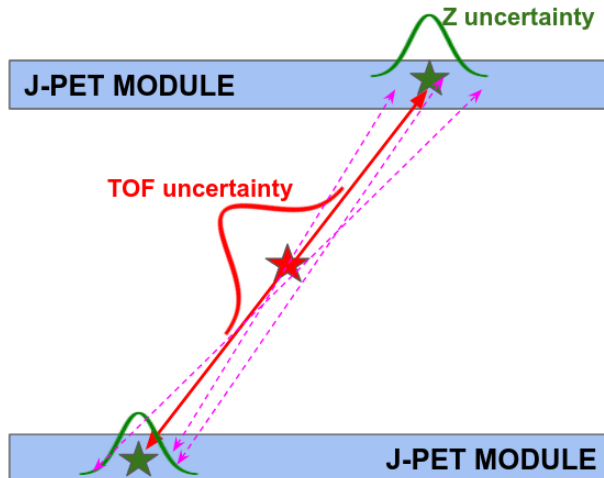


Figure 2: TOF uncertainty sources in the J-PET scanner. Apart from the uncertainty along the line of response (marked in red), additional distortion due to the hit registration resolution along the plastic scintillator (green) is present. Exemplary lines of responses are shown in violet.

consequence, it is expected that the optimal width of the shift-invariant Gaussian kernel will be broader than the one determined based solely on the scintillator time resolution properties. Therefore in the first step, we performed an investigation to select an optimal shift-invariant Gaussian kernel width. The studies were repeated for all setups, to ensure that the common kernel can be chosen. The selected kernel parameters were applied in all subsequent image reconstruction studies.

III.E. System sensitivity and image quality metrics

The performance of the scanners has been evaluated based on several criteria including the sensitivity profiles and image quality metrics.

The sensitivity of the scanner S is defined as the rate of detected true coincidences (counts per s) per unit of the radioactivity concentration. The Monte-Carlo determined (S_{MC}) sensitivity in the peak, was compared with the calculated theoretical (S_{theor}) value. For that, the geometrical acceptance, detection efficiency of the photon pair, the fraction of events accepted after applying the energy window and the factor accounts for the holes and

inactive detector components were considered. In the Supplementary Materials extended explanation of the theoretical sensitivity calculation is given.

The evaluation of the reconstruction performance is based on the metrics defined in the NEMA NU 2–2018 norm for image quality assessment⁶⁰. The procedure is to choose two types of ROIs within the reconstructed image and determine their statistical properties. The first ROI corresponds to the expected high activity (*hot*) signal region and the second ROI corresponds to low activity background region(s) ROI. The *CRC* for a given region of interest is defined as:

$$CRC = \frac{C_S - C_B}{C_B} : \frac{a_S - a_B}{a_B}, \quad (1)$$

where C_S , C_B is the average number of counts determined for signal and background ROI, and a_S , a_B are the signal and background activities, respectively.

The *BV* is defined as a standard deviation (S_B) calculated for the background ROI normalized to the average counts in the background region:

$$BV = \frac{S_B}{C_B}. \quad (2)$$

We inspected the additional metric *Q*, which combines the information from both, *CRC* and *BV*, and is defined as³⁴:

$$Q = |CRC - 1| + BV. \quad (3)$$

The *Q* value range is given by: $Q \in [0, \infty)$. For the perfect image reconstruction in terms of *CRC* and *BV*, one expects 1 and 0 for *CRC* and *BV*, respectively. By definition, *Q* would also be equal to 0.

We defined the *RMSE* between two images I_1 and I_2 is defined as:

$$RMSE[I_1, I_2] = \frac{1}{N} \sqrt{\sum_{k=1}^N (I_1[k] - I_2[k])^2}, \quad (4)$$

where N is the total number of voxels, respectively.

In our studies, the activity emission map was used as a ground-truth reference image. Before the *RMSE* calculation, the compared reference and reconstructed images were first normalized to the maximum. Then, the median intensities were calculated for both. Background activity and whole phantom areas were used to calculate medians. Subsequently, the ratio between medians was calculated and finally, the original image was scaled by the ratio.

III.F. Metric uncertainty estimation

We use the bootstrap resampling method^{61,62} to assess the uncertainty of the calculated metrics. Our implementation follows the list-mode-based nonparametric approach proposed in the PET context by the work⁶³ and further discussed in the articles^{64,65}, in which a new sample is formed by randomly choosing events with replacement from the original coincidence list obtained from the MC simulations. For each distinctive scenario defined by phantom, scanner setup and parameter settings, 20 bootstrapped samples were prepared and reconstructed. The target metrics values together with their uncertainties are estimated by averaging over the set of bootstrapped realizations.

IV. Results

IV.A. Sensitivity for two-gamma tomography

Sensitivity plots for all simulated scanners are shown in Fig. 3. The characteristic "spikes"

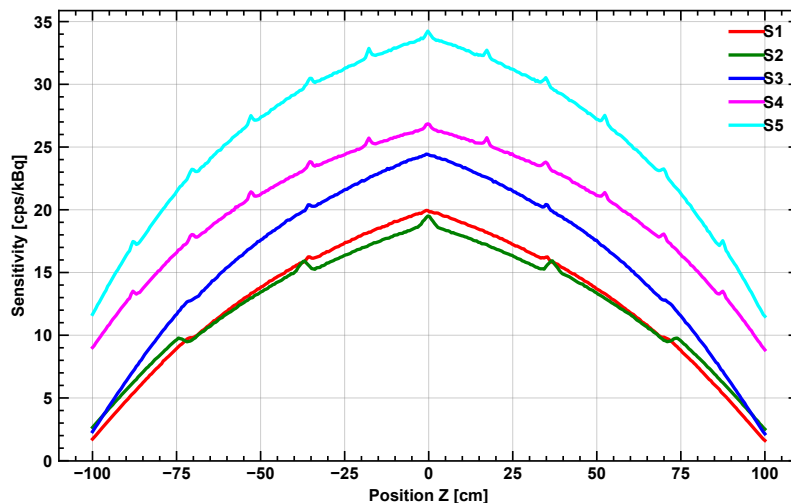


Figure 3: Sensitivity profiles for tested TB J-PET geometries.

visible in the sensitivity profiles correspond to the centres of the strips and the gaps between adjacent rings. The sensitivity values in the peak are compared with the analytical calculations in Table 2. The Monte Carlo-based results are in reasonable agreement with the analytical calculations. The slight underestimation of the analytical calculations compared to the Monte Carlo ones can be explained by the estimation method of the packing factor,

Table 2: Theoretical (S_{theor}) and Monte Carlo-calculated (S_{MC}) sensitivity in the peak of the sensitivity profile for the source positioned in the scanner centre.

Type	S_{theor} [cps/kBq]	S_{MC} [cps/kBq]
S1	17.61	19.95
S2	17.21	19.50
S3	22.69	24.44
S4	23.21	26.85
S5	30.57	34.24

which accounts for holes and inactive detector components without taking into account the depth of the crystal in the estimation. A detailed explanation of the analytical estimation method can be found in the Supplementary Materials. Overall, the greatest sensitivity has been found for the scanner S5 with the maximum at the level of 34 cps/kBq. The lowest values are observed for the scanners S1 and S2 with the maximum at the level of 17 cps/kBq. The observed difference is a simple consequence of the higher geometrical coverage of the S5 scanner due to its smaller radius and larger AFOV.

IV.B. Sensitivity for the positronium tomography

The Monte Carlo-based sensitivity plots and sensitivity in peak values for all simulated scanners are shown in Fig. 4 and Table 3, respectively.

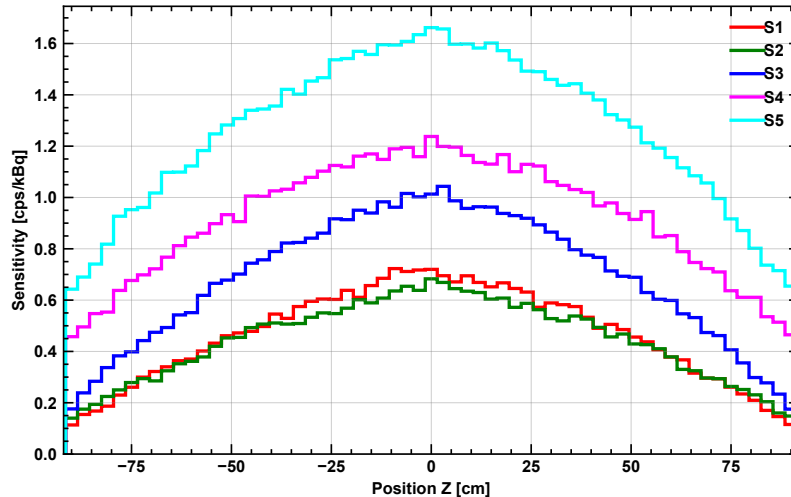


Figure 4: Multi-gamma imaging sensitivity profiles for tested TB J-PET geometries.

The profiles are characterized by the same trend as for the two-gamma sensitivity. The

Table 3: Monte Carlo-calculated ($S_{MC_{2+1}}$) sensitivity in the peak of the sensitivity profile for the source 2+1 positioned in the scanner centre.

Type	$S_{MC_{2+1}}$ [cps/kBq]
S1	0.72
S2	0.68
S3	1.01
S4	1.24
S5	1.66

Table 4: Number of true, scatter and random coincidences.

Type	XCAT [10^7]		
	True	Scatter	Random
S1	5.7	3.9	6.0
S2	5.5	3.7	5.8
S3	8.2	6.1	9.1
S4	9.7	7.2	10.6
S5	12.6	9.5	13.5

greatest values are observed for the S5 scanner (1.66 cps/kBq in peak). On the other hand, the lowest values are observed for the S2 scanner with the maximum at the level of 0.68 cps/kBq. The sensitivity (in the peak) for positronium tomography is about 20-30 times lower than the sensitivity for the two-gamma imaging.

IV.C. Number of coincidences

The numbers of coincidences registered for two-gamma tomography for each scanner and XCAT phantoms are of the order of 10^7 - 10^8 and are given in Table 4. The greatest number is found for the S5 scanner and the smallest for the S1 scanner. It is an effect of the increased geometrical acceptance and detector efficiency for the thicker (S5 scanner) scintillator layer.

IV.D. Choice of the optimal TOF kernel

The nominal TOF resolution estimated based on the time-smearing parameters set in the simulations with the scanner S5 corresponds to FWHM of about 166 ps (see Supplementary Materials). The comparison of the images reconstructed with various Gaussian kernel widths is presented in Fig. 5. The visual inspection reveals that the reconstruction with smaller

kernel widths (TOF = 115 ps and TOF = 230 ps) generates images with higher background and noise levels. Furthermore, the contrast between hot regions and the background is clearer for the images reconstructed with a broader TOF width. These conclusions are confirmed

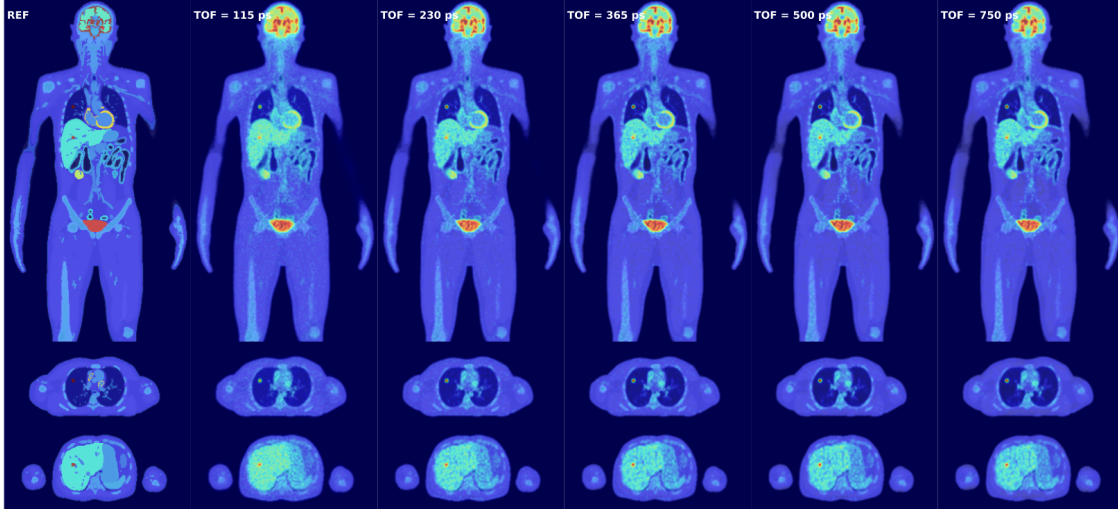


Figure 5: Simulated (REF label) and reconstructed XCAT phantom images (TOF label) for five different Gaussian TOF kernel widths for the sagittal (top panel) and axial (center and bottom panel) views. The center and bottom panels show the slice through the hot spot in the lungs and liver, respectively. PET images are overlaid onto CT scans. Given slices are for S5. 30th iteration images are shown.

by analysing the Q distribution as a function of iteration and applied TOF kernel width presented in Fig. 6. The Q is determined for hot spots. It is found that in all cases the best Q values are observed for the TOF kernel width broader than 230 ps. For five out of six cases (excluding hot spot positioned in the liver) the lowest (the best) Q are found for the TOF = 365 ps and TOF = 500 ps. The TOF = 115 ps obtained the highest (worse) Q characteristic among all the presented cases. It is also noticeable that for all the images for 50th iteration the Q metric reaches the plateau. The same trend was observed for other scanners. Corresponding plots are included in the Supplementary Materials.

Taking into account both, the visual inspection and quantitative results, the range of the TOF kernel width between 365 ps to 750 ps gives the best results. The shapes of the metric plots are very similar and they are preserved for all the scanners. In the further image quality analysis, we proceed with the images reconstructed with the common Gaussian kernel width set to 500 ps.

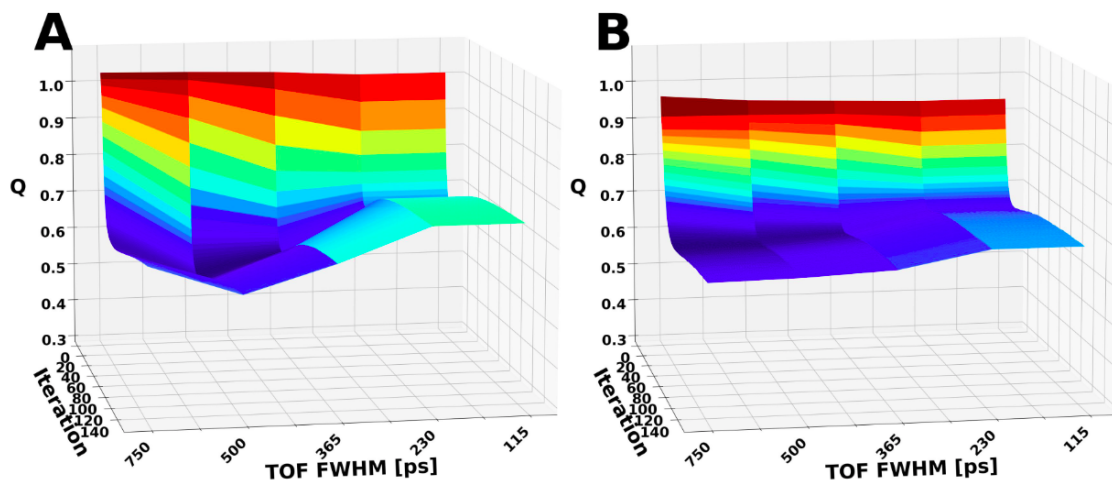


Figure 6: The Q metric distributions for lungs (panel A) and liver (panel B) for the scanner S5.

IV.E. Image Quality

Fig. 7 presents the images for all the scanners after 30 iterations. The visual inspection indicates that the background noise is higher for the S1, S2 and S3 scanners. It is particularly visible in the shoulder girdles and in the axial slices with hot spots in the lungs and the liver. At the same time, the contrast values are similar for all investigated scanners.

A comprehensive analysis of CRC, BV, Q and RMSE metrics is presented in Fig. 8. The greatest CRC value is observed for the lungs, although the CRC variation for each ROI among the scanners does not exceed two standard deviations. Vast discrepancies are observed for the BV metrics. Here, scanners S4 and S5 show statistically significant superiority for both the liver and the lung regions over the rest of the scanners. At the same time, the worst results are found for the scanners with the greatest radius - S1 and S2. Above mentioned findings are reflected in the Q metric. As in the case of the BV, the S5 scanner is characterized by the lowest Q metric for both - the liver and the lungs. The same trend is observed for the RMSE metric where the scanner S5 shows an advantage over the results of the other scanners. It can be observed in the liver region. The performance of scanners S1 and S2 is significantly worse than the other scanners. The obtained quantitative results are in agreement with the qualitative, visual inspection.

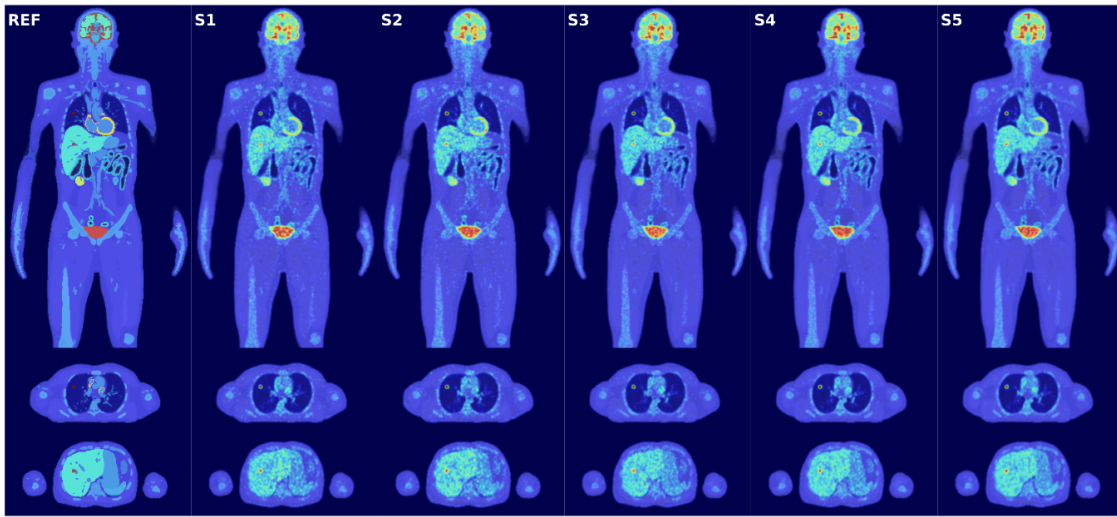


Figure 7: Simulated (REF panel) and reconstructed (S1-S5) XCAT phantom images for five different scanner types for the sagittal (top panel) and axial (center and bottom panel) views. The center and bottom panels show the slices through the hot spot in the lungs and liver, respectively. PET images are overlaid onto CT scans. For each scanner, the 30th iteration image is shown.

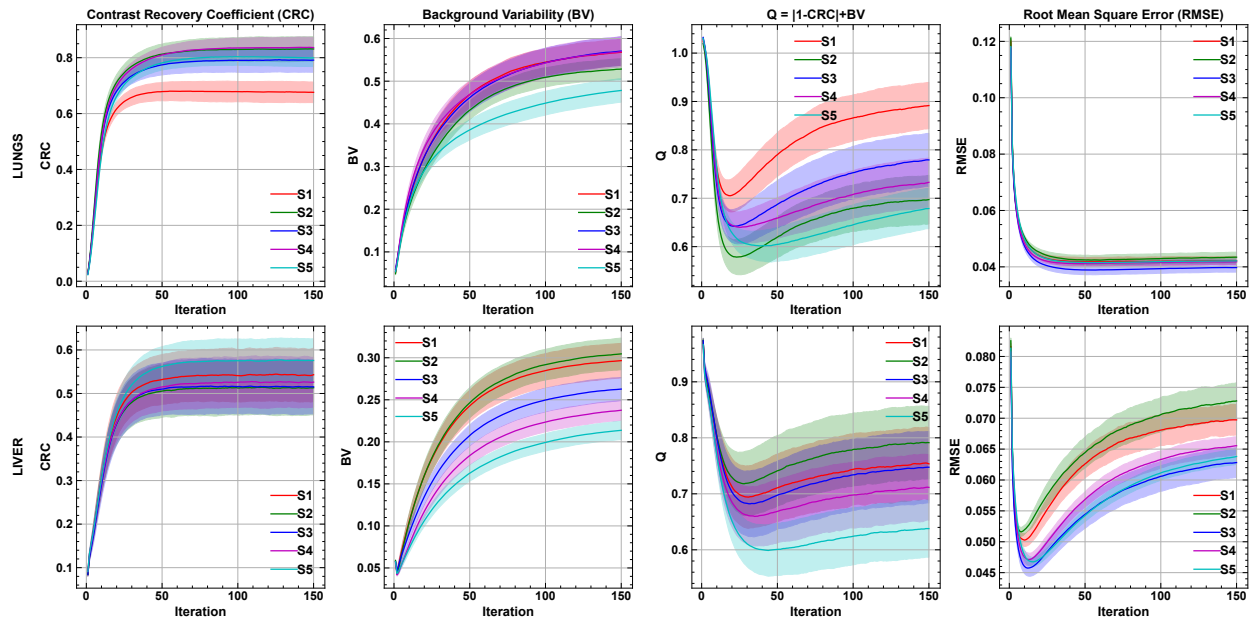


Figure 8: CRC (first column), BV (second column), Q (third column) and RMSE (fourth column) characteristics for the liver (top row) and lungs (bottom row) regions calculated based on the reconstructed XCAT phantom images for all five scanners. Shaded regions indicate the one standard deviation region.

V. Discussion

The most important characteristics determined for the studied scanners are gathered in Table 5.

In the presented study two-gamma sensitivity profiles for five total-body J-PET scanner geometries (Table 1 and 5) were determined. The peak sensitivity values vary from 20 to 34 cps per kBq and are dominated by the differences in the geometrical acceptance of the scanners. The maximum peak sensitivity of 34 cps per kBq was found for the scanner S5. This value is slightly lower than the result reported in our previous study²⁴, where for the 200 cm ideal scanner the sensitivity in peak is equal to 38 cps per kBq. The difference can be explained by the larger radius of the investigated setup (41.4 cm versus 39 cm) and the inclusion of the gaps between rings and adjacent plastic scintillators. Contrasted with the values reported for the state-of-the-art TB scanners: uExplorer (191.5 cps per kBq) and PennPET (55 cps per kBq)⁸, the J-PET scanner sensitivity is lower, however, it can be seen as a significant improvement concerning the current 16–26 cm long PET systems³⁶.

The sensitivity curves for the positronium tomography have a similar shape to the two-gamma sensitivity profiles. Since they are calculated based on the triple coincidences formed by the two annihilation and one deexcitation photons, the values in the peak are much lower compared to the two-gamma cases, from about 28 times lower for the S1 and S2 scanners to about 20 times lower for the S5 scanner. One can observe, that the sensitivity for triple coincidences rises much faster as a function of AFOV than the corresponding dependence for the two-gamma case. The sensitivity in the peak for positronium imaging rises by 130% comparing the S5 to S1 scanner. On the other hand, the two-gamma sensitivity in the peak Table 5: Price reduction factor compared to the Explorer material budget, sensitivity in the peak for the two-gamma (S_{MC}) and the two+one ($S_{MC_{2+1}}$) sources positioned in the scanner centre, CRC, BV, and Q metrics for the 150th iteration in lungs and liver areas.

Type	Price factor	S_{MC} [cps/kBq]	$S_{MC_{2+1}}$ [cps/kBq]	CRC_{lungs}	CRC_{liver}	BV_{lungs}	BV_{liver}	Q_{lungs}	Q_{liver}
S1	9.6	19.95	0.72	0.68(4)	0.54(6)	0.57(3)	0.30(2)	0.89(5)	0.75(6)
S2	9.6	19.50	0.68	0.83(4)	0.51(6)	0.53(2)	0.30(2)	0.70(5)	0.79(6)
S3	9.6	24.44	1.01	0.79(4)	0.52(6)	0.57(3)	0.26(1)	0.78(5)	0.75(6)
S4	4.3	26.85	1.24	0.84(4)	0.53(6)	0.57(3)	0.24(1)	0.73(5)	0.71(6)
S5	3.6	34.24	1.66	0.80(3)	0.58(5)	0.48(3)	0.21(1)	0.68(4)	0.64(5)

gain raises by only 70% from S1 to S5.

The highest peak sensitivity for positronium imaging is estimated for the S5 scanner and is equal to 1.66 cps/kBq. This value can be contrasted with the estimated sensitivity of the positronium imaging in the peak of 0.06 cps/kBq of the J-PET modular scanner, which has been used to reconstruct the first positronium mean lifetime image of the human brain in vivo⁶⁶. This makes the J-PET TB modality a well-suited scanner for multi-photon imaging^{13,25}.

The quantitative analysis of the reconstructed image quality was performed based on simulations of the XCAT phantom. The analysis of the reconstructed images confirms the feasibility of multi-organ imaging with J-PET TB technology. The visual inspection reveals the superiority of the seven-ring scanners (S4 and S5) over the three-ring setups (S1, S2 and S3) (Fig. 7). In particular, the noise level is smaller for the scanners S4 and S5. This is confirmed by the quantitative results shown in Fig. 8 and in Table 5. The BV value for the S5 is the lowest for both lesions. BV values are of a similar order as the CRC ones. Thus, both BV and CRC will have similar importance in the Q metric results. For this case, the Q value indicates the scanners S4 and S5 are the optimal geometries for a Total-Body J-PET. Additionally, the RMSE characteristics (for the liver lesions specifically) show the scanners S4 and S5 to best mimic the simulated reference image.

In our study, the simulated scenarios use the same overall activity between investigated scanners and the acquisition time for all the scanners to better reproduce the real conditions. As a consequence, the reconstructed images and calculated metrics differ in the number of registered coincidences. It is plausible that the effect of the reduced background variability can be fully explained by the higher statistics acquired by the scanners S4 and S5.

Note that the presented reconstruction and analysis protocols require further optimization for potential clinical application and it is out of the scope of this paper.

V.A. Limitations

In the image reconstruction process, the sensitivity and attenuation corrections were included. Image quality could be further improved by the addition of other correction factors such as point spread function (PSF) or depth-of-interaction (DOI) modelling. Indeed, the ef-

forts to develop a dedicated J-PET system response matrix are ongoing⁵⁸. Also, no selection criteria for the obliqueness of the accepted line-of-responses were applied. As shown in our previous study, it could improve the contrast and background of the reconstructed images⁶⁷. However, the more accurate system matrix modelling or application of the obliqueness selection criteria would improve the overall metric values e.g. contrast, but would not change the relative trends we observed among the scanner setups.

In our study, only the true coincidences were used for the image reconstruction. Further studies must be carried out to develop the scatter and random correction methods for the J-PET-based TB scanners.

VI. Conclusions

We performed comparative studies of five realistic, two-layer TB J-PET scanners, based on the Monte Carlo simulations of the XCAT phantom. The overall performance was quantified in terms of CRC, BV, Q and RMSE metrics for the two-gamma tomography. In addition, the two-gamma and positronium imaging sensitivity curves were determined. The results show the feasibility of multi-organ imaging of all the systems to be considered for the next generation of TB J-PET designs.

Among the scanner parameters, the most important ones are related to the axial FOV coverage. The influence of the time resolution depending on the scintillator length, positional uncertainty due to different material thickness and other parameters have a secondary effect on the reconstruction quality within the considered values range, and are dominated by the parameters related to the overall registration efficiency such as total length of the active material or scanner radius. It can be concluded that the image quality increases for the higher two-gamma sensitivity scanners and is manifested mainly in the lower background variability values due to the higher statistics acquired. A similar effect was observed in analysing the data from the uExplorer TB PET scanner⁵⁶. The two-gamma sensitivity and XCAT image reconstruction analyses in terms of the quality metrics, together with the visual inspection of the reconstructed images show the advantage of longer, seven-ring S4 and S5 scanners. However, the improvement comes with a higher price. As estimated, the cost of the scintillator materials and SiPMs which constitute a majority of the TB price is more

than two times higher for the S4, and S5 modalities compared to the three-ring solutions. Still, the relative cost for all the scanners is about 10 to 4 times lower compared to the cost of the uExplorer modality.

The importance of the high-sensitivity systems becomes more pronounced in the case of the positronium mean lifetime tomography which requires the registration of triple gamma coincidences. The determined positronium sensitivity values make the J-PET TB modality a well-suited scanner for positronium lifetime imaging^{13,66}. It is worth underlining that the positronium lifetime tomography is well suited to be performed on other high-sensitivity, large FOV scanners such as Biograph Vision Quadra or uExplorer. However, it requires operating on the single acquisition mode that permits to registration of multi-gamma coincidences. This condition can pose problems, especially for the system approved for clinical usage.

The enumerated properties together with its cost-effectiveness and triggerless acquisition mode enabling three gamma positronium imaging, make the J-PET technology an attractive solution for broad application in clinics.

VII. Acknowledgments

The authors gratefully acknowledge the support of the Foundation for Polish Science through programme TEAM POIR.04.04.00-00-4204/17; the National Science Centre of Poland through grant nos. 2019/35/B/ST2/03562, 2020/38/E/ST2/00112, 2021/42/A/ST2/00423 and 2021/43/B/ST2/02150; the Ministry of Education and Science under the grant No. SPUB/SP/490528/2021 and IAL/SP/596235/2023; EU Horizon 2020 research and innovation programme, STRONG-2020 project, under grant agreement No 824093; the Jagiellonian University via the project CRP/0641.221.2020, and via SciMat and qLife Priority Research Areas under the program Excellence Initiative-Research University at the Jagiellonian University.

VIII. Conflict of Interest Statement

The Authors declare no conflict of interest.

References

- ¹ Schmall J. P., Karp J. S. and Alavi A., The potential role of total body PET imaging in assessment of atherosclerosis, *PET clinics* **14**, 245–250 (2019).
- ² A. Alavi, T. J. Werner, E. Stepień, and P. Moskal, Unparalleled and revolutionary impact of PET imaging on research and day to day practice of medicine, *Bio-Algorithms and Med-Systems* **17**, 203–212 (2021).
- ³ A. Alavi, S. Hess, T. J. Werner, and P. F. Høilund-Carlsen, An update on the unparalleled impact of FDG-PET imaging on the day-to-day practice of medicine with emphasis on management of infectious/inflammatory disorders, 2020.
- ⁴ Cherry S. R., Badawi R. D., Karp J. S. et al., Total-body imaging: Transforming the role of positron emission tomography, *Science Translational Medicine* **9**, eaaf6169 (2017).
- ⁵ B. A. Spencer et al., Performance evaluation of the uEXPLORER total-body PET/CT scanner based on NEMA NU 2-2018 with additional tests to characterize PET scanners with a long axial field of view, *Journal of Nuclear Medicine* **62**, 861–870 (2021).
- ⁶ Karp J. S., Viswanath V., Geagan M. J. et al., PennPET Explorer: design and preliminary performance of a whole-body imager, *Journal of Nuclear Medicine* **61**, 136–143 (2020).
- ⁷ G. A. Prenosil, H. Sari, M. Fürstner, A. Afshar-Oromieh, K. Shi, A. Rominger, and M. Hentschel, Performance Characteristics of the Biograph Vision Quadra PET/CT System with a Long Axial Field of View Using the NEMA NU 2-2018 Standard, *Journal of nuclear medicine* **63**, 476–484 (2022).
- ⁸ S. Vandenberghe, P. Moskal, and J. S. Karp, State of the art in total body PET, *EJNMMI physics* **7**, 1–33 (2020).
- ⁹ S. Vandenberghe, N. A. Karakatsanis, M. A. Akl, J. Maebe, S. Surti, R. A. Dierckx, D. A. Pryma, S. A. Nehmeh, O. Bouhali, and J. S. Karp, The potential of a medium-cost long axial FOV PET system for nuclear medicine departments, *European Journal of Nuclear Medicine and Molecular Imaging* **50**, 652–660 (2023).
- ¹⁰ X. Zhang et al., Total-body dynamic reconstruction and parametric imaging on the uEXPLORER, *Journal of Nuclear Medicine* **61**, 285–291 (2020).

-
- ¹¹ G. Wang, L. Nardo, M. Parikh, Y. G. Abdelhafez, E. Li, B. A. Spencer, J. Qi, T. Jones, S. R. Cherry, and R. D. Badawi, Total-Body PET Multiparametric Imaging of Cancer Using a Voxelwise Strategy of Compartmental Modeling, *Journal of Nuclear Medicine* **63**, 1274–1281 (2022).
 - ¹² P. Moskal et al., Positronium imaging with the novel multiphoton PET scanner, *Science Advances* **7**, eabh4394 (2021).
 - ¹³ P. Moskal and E. Ł. Stepień, Perspectives for translation of positronium imaging into clinics, *Frontiers in Physics* , 891 (2022).
 - ¹⁴ Moskal P., Kisielewska D., Curceanu C. et al., Feasibility study of the positronium imaging with the J-PET tomograph, *Physics in Medicine and Biology* **64**, 055017 (2019).
 - ¹⁵ E. Y. Beyene et al., Exploration of simultaneous dual-isotope imaging with multi-photon modular J-PET scanner, *Bio-Algorithms and Med-Systems* **19** (2023).
 - ¹⁶ Cherry S. R., Jones T., Karp J. S. et al., Total-Body PET: Maximizing Sensitivity to Create New Opportunities for Clinical Research and Patient Care, *The Journal of Nuclear Medicine* **59**, 3–12 (2018).
 - ¹⁷ Surti S., Pantel A. R. and Karp J. S., Total Body PET: Why, How, What for?, *IEEE Transactions on Radiation and Plasma Medical Sciences* **4**, 283–292 (2020).
 - ¹⁸ Surti S., Werner M. E. and Karp J. S., Study of PET scanner designs using clinical metrics to optimize the scanner axial FOV and crystal thickness, *Physics in Medicine and Biology* **58**, 3995 (2013).
 - ¹⁹ Zhang J., Knopp M. I. and Knopp M. V., Sparse detector configuration in SiPM digital photon counting PET: a feasibility study, *Molecular Imaging and Biology* **21**, 447–453 (2019).
 - ²⁰ Zein S. A., Karakatsanis N. A., Issa M. et al., Physical performance of a long axial field-of-view PET scanner prototype with sparse rings configuration: A Monte Carlo simulation study, *Medical Physics* **47**, 1949–1957 (2020).
 - ²¹ Cates J. W. and Levin C. S., Electronics method to advance the coincidence time resolution with bismuth germanate, *Physics in Medicine and Biology* **64**, 175016 (2019).
-

- ²² Gundacker S., Turtos R. M., Kratochwil N., et al., Experimental time resolution limits of modern SiPMs and TOF-PET detectors exploring different scintillators and Cherenkov emission, *Physics in Medicine and Biology* **65**, 025001 (2020).
- ²³ Kowalski P., Wiślicki W., Shopa R. Y. et al., Estimating the NEMA characteristics of the J-PET tomograph using the GATE package, *Physics in Medicine and Biology* **63**, 165008 (2018).
- ²⁴ P. Moskal et al., Simulating NEMA characteristics of the modular total-body J-PET scanner—an economic total-body PET from plastic scintillators, *Physics in Medicine and Biology* **66**, 175015 (2021).
- ²⁵ P. Moskal and E. Stepień, Prospects and clinical perspectives of total-body PET imaging using plastic scintillators, *PET Clinics* **15**, 439–452 (2020).
- ²⁶ F. Tayefi Ardebili, S. Niedźwiecki, and P. Moskal, Evaluation of modular J-PET sensitivity, *Bio-Algorithms and Med-Systems* **19** (2023).
- ²⁷ Hiesmayr B. C. and Moskal P., Witnessing entanglement in Compton scattering processes via mutually unbiased bases, *Scientific Reports* **9**, 1–14 (2019).
- ²⁸ P. Moskal et al., Testing CPT symmetry in ortho-positronium decays with positronium annihilation tomography, *Nature Commun.* **12**, 5658 (2021).
- ²⁹ P. Moskal et al., Discrete symmetries tested at 10⁻⁴ precision using linear polarization of photons from positronium annihilations, *Nature Communications* **15**, 78 (2024).
- ³⁰ J. Baran, J. Gajewski, M. Pawlik-Niedźwiecka, P. Moskal, and A. Ruciński, Studies of J-PET detector to monitor range uncertainty in proton therapy, in *2019 IEEE Nuclear Science Symposium and Medical Imaging Conference (NSS/MIC)*, pages 1–4, IEEE, 2019.
- ³¹ J. Baran et al., Feasibility of the J-PET to monitor the range of therapeutic proton beams, *Physica Medica* **118**, 103301 (2024).
- ³² D. Borys et al., ProTheRaMon—a GATE simulation framework for proton therapy range monitoring using PET imaging, *Physics in Medicine and Biology* **67**, 224002 (2022).

-
- ³³ K. W. Brzezinski et al., Detection of range shifts in proton beam therapy using the J-PET scanner: a patient simulation study, *Physics in Medicine and Biology* **68**, 145016 (2023).
- ³⁴ R. Y. Shopa et al., Optimisation of the event-based TOF filtered back-projection for online imaging in total-body J-PET, *Medical Image Analysis* **73**, 102199 (2021).
- ³⁵ L. Raczyński et al., 3D TOF-PET image reconstruction using total variation regularization, *Physica Medica* **80**, 230–242 (2020).
- ³⁶ Moskal P., Kisielewska D., Shopa R. Y. et al., Performance assessment of the 2 γ positronium imaging with the total-body PET scanners, *EJNMMI Phys.* **7**, 44 (2020).
- ³⁷ K. Shibuya, H. Saito, F. Nishikido, M. Takahashi, and T. Yamaya, Oxygen sensing ability of positronium atom for tumor hypoxia imaging, *Communications Physics* **3**, 1–8 (2020).
- ³⁸ T. Yamaya, E. Yoshida, N. Inadama, F. Nishikido, K. Shibuya, M. Higuchi, and H. Murayama, A multiplex “OpenPET” geometry to extend axial FOV without increasing the number of detectors, *IEEE Transactions on Nuclear Science* **56**, 2644–2650 (2009).
- ³⁹ M. E. Daube-Witherspoon, V. Viswanath, M. E. Werner, and J. S. Karp, Performance characteristics of long axial field-of-view PET scanners with axial gaps, *IEEE Transactions on Radiation and Plasma Medical Sciences* **5**, 322–330 (2020).
- ⁴⁰ J. Smyrski et al., Measurement of gamma quantum interaction point in plastic scintillator with WLS strips, *Nuclear Instruments and Methods in Physics Research Section A: Accelerators, Spectrometers, Detectors and Associated Equipment* **851**, 39–42 (2017).
- ⁴¹ S. Niedźwiecki et al., J-PET: a new technology for the whole-body PET imaging, *Acta Phys. Polon.* **B48**, 1567 (2017).
- ⁴² M. T. Kaplanoglu and P. Moskal, A cross-staged gantry for total-body PET and CT imaging, *Bio-Algorithms and Med-Systems* **19** (2023).
- ⁴³ D. Sarrut et al., Advanced Monte Carlo simulations of emission tomography imaging systems with GATE, *Physics in Medicine & Biology* **66**, 10TR03 (2021).
-

- ⁴⁴ D. Sarrut et al., The OpenGATE ecosystem for Monte Carlo simulation in medical physics, *Physics in Medicine and Biology* **67**, 184001 (2022).
- ⁴⁵ S. Agostinelli et al., GEANT4—a simulation toolkit, *Nuclear instruments and methods in physics research section A: Accelerators, Spectrometers, Detectors and Associated Equipment* **506**, 250–303 (2003).
- ⁴⁶ W. P. Segars, G. Sturgeon, S. Mendonca, J. Grimes, and B. M. Tsui, 4D XCAT phantom for multimodality imaging research, *Medical physics* **37**, 4902–4915 (2010).
- ⁴⁷ S. Zincirkeser, E. Şahin, M. Halac, and S. Sager, Standardized uptake values of normal organs on 18F-fluorodeoxyglucose positron emission tomography and computed tomography imaging, *Journal of international medical research* **35**, 231–236 (2007).
- ⁴⁸ J. Silva-Rodríguez, P. Aguiar, I. Domínguez-Prado, P. Fierro, and Á. Ruibal, Simulated FDG-PET studies for the assessment of SUV quantification methods, *Revista Española de Medicina Nuclear e Imagen Molecular (English Edition)* **34**, 13–18 (2015).
- ⁴⁹ L. Raczyński et al., Calculation of the time resolution of the J-PET tomograph using kernel density estimation, *Physics in Medicine & Biology* **62**, 5076 (2017).
- ⁵⁰ S. Vandenberghe, P. Moskal, and J. Karp, State of the art in total body PET, *EJNMMI-Physics* **7**, 35 (2020).
- ⁵¹ J. Thatcher and M. Osman, Prevalence, challenges and solutions for F-18 FDG PET/CT imaging of claustrophobic patients, *Journal of Nuclear Medicine* **47**, 558P–558P (2006).
- ⁵² P. Moskal et al., Test of a single module of the J-PET scanner based on plastic scintillators, *Nucl. Instrum. Meth.* **A764**, 317–321 (2014).
- ⁵³ P. Moskal et al., Time resolution of the plastic scintillator strips with matrix photomultiplier readout for J-PET tomograph, *Physics in Medicine & Biology* **61**, 2025 (2016).
- ⁵⁴ Moskal P., Alfs D., Bednarski T. et al., Potential of the J-PET detector for studies of discrete symmetries in decays of positronium atom—a purely leptonic system, *Acta Phys. Polon.* **B47**, 509 (2016).

-
- ⁵⁵ Moskal P., Krawczyk N., Hiesmayr B. C. et al., Feasibility studies of the polarization of photons beyond the optical wavelength regime with the J-PET detector, *The European Physical Journal C* **78**, 970 (2018).
- ⁵⁶ X. Zhang, J. Zhou, S. R. Cherry, R. D. Badawi, and J. Qi, Quantitative image reconstruction for total-body PET imaging using the 2-meter long EXPLORER scanner, *Physics in Medicine & Biology* **62**, 2465 (2017).
- ⁵⁷ T. Merlin, S. Stute, D. Benoit, J. Bert, T. Carlier, C. Comtat, M. Filipovic, F. Lamare, and D. Visvikis, CASToR: a generic data organization and processing code framework for multi-modal and multi-dimensional tomographic reconstruction, *Physics in Medicine & Biology* **63**, 185005 (2018).
- ⁵⁸ R. Shopa et al., TOF MLEM Adaptation for the Total-Body J-PET with a Realistic Analytical System Response Matrix, *IEEE Transactions on Radiation and Plasma Medical Sciences* (2023).
- ⁵⁹ M. E. Daube-Witherspoon, S. Surti, S. Matej, M. Werner, S. Jayanthi, and J. S. Karp, Influence of time-of-flight kernel accuracy in TOF-PET reconstruction, in *2006 IEEE Nuclear Science Symposium Conference Record*, volume 3, pages 1723–1727, IEEE, 2006.
- ⁶⁰ NEMA, NEMA Standards Publication NU 2-2018: Performance Measurements of Positron Emission Tomographs (PET), 2018, National Electrical Manufacturers Association (NEMA NU 2-2018).
- ⁶¹ B. Efron, Bootstrap methods: another look at the jackknife, in *Breakthroughs in statistics: Methodology and distribution*, pages 569–593, Springer, 1992.
- ⁶² B. Efron and R. J. Tibshirani, *An Introduction to the Bootstrap*, Springer US.
- ⁶³ M. Dahlbom, Estimation of image noise in PET using the bootstrap method, in *2001 IEEE Nuclear Science Symposium Conference Record (Cat. No. 01CH37310)*, volume 4, pages 2075–2079, IEEE, 2001.
- ⁶⁴ C. Lartizien, J.-B. Aubin, and I. Buvat, Comparison of Bootstrap Resampling Methods for 3-D PET Imaging, **29**, 1442–1454.
-

- ⁶⁵ P. Markiewicz, A. Reader, and J. Matthews, Assessment of bootstrap resampling performance for PET data, *Physics in Medicine and Biology* **60**, 279–299 (2015).
- ⁶⁶ P. Moskal et al., First positronium image of the human brain in vivo, medRxiv preprint medRxiv:<https://doi.org/10.1101/2024.02.01.23299028> (2024).
- ⁶⁷ P. Kopka and K. Klimaszewski, RECONSTRUCTION OF THE NEMA IEC BODY PHANTOM FROM J-PET TOTAL-BODY SCANNER SIMULATION USING STIR., *Acta Physica Polonica B* **51**, 357 (2020).

List of Figures

1	Visualisation of the scanner geometry.	7
2	TOF uncertainty sources in the J-PET scanner. Apart from the uncertainty along the line of response (marked in red), additional distortion due to the hit registration resolution along the plastic scintillator (green) is present. Exemplary lines of responses are shown in violet.	9
3	Sensitivity profiles.	11
4	Sensitivity profiles.	12
5	Reconstructed XCAT images for five different Gaussian TOF widths for S5 scanner.	14
6	The Q metric for the S5 scanner.	15
7	Reconstructed XCAT images for five different scanners with Gaussian TOF kernel width equal to 500 ps.	16
8	CRC, BV, Q and RMSE metrics for XCAT for different scanners.	16